

The Discrepant Kinematics of ORLs and CELs in NGC 7009 as a Function of Ionization Structure ¹

Michael G. Richer¹, Leonid Georgiev^{2†}, Anabel Arrieta³, and Silvia Torres-Peimbert²

¹ *Instituto de Astronomía, Universidad Nacional Autónoma de México, Apartado Postal 106, 22800 Ensenada, BC, México; richer@astrocen.unam.mx*

² *Instituto de Astronomía, Universidad Nacional Autónoma de México, Apartado Postal 70 - 264, México, DF, CP 04510; silvia@astroscu.unam.mx*

³ *Universidad Iberoamericana, Departamento de Física y Matemáticas, Prolongación Paseo de la Reforma 880, Lomas de Santa Fe, CP 01210 México DF, México; anabel.arrieta@ibero.mx*

ABSTRACT

We present spatially- and velocity-resolved echelle spectroscopy for NGC 7009 obtained with the UVES spectrograph at the European Southern Observatory's Very Large Telescope. Our objective is to analyze the kinematics of emission lines excited by recombination and collisions with electrons to determine whether similarities or differences could be useful in elucidating the well-known abundance discrepancy derived from them. We construct position-velocity maps for recombination, fluorescence, charge transfer, and collisionally-excited lines. We find a plasma component emitting in the C II, N II, O II, and Ne II recombination lines whose kinematics are discrepant: They are incompatible with the ionization structure derived from all other evidence and the kinematics derived from all of these lines are unexpectedly very similar. We find direct evidence for a recombination contribution to [N II] λ 5755. Once taken into account, the electron temperatures from [N II], [O III], and [Ne III] agree at a given position and velocity. The electron densities derived from [O II] and [Ar IV] are consistent with direct imaging and the distribution of hydrogen emission. The kinematics of the C II, N II, O II, and Ne II lines *does not* coincide with the kinematics of the [O III] and [Ne III] forbidden emission, indicating that there is an additional plasma component to the recombination emission that arises from a different volume from that giving rise to the forbidden emission from the parent ions within NGC 7009. Thus, the chemical abundances derived from either type of line are correct only for the plasma component from which they arise. Apart from [N II] λ 5755, we find no anomaly with the forbidden lines usually used to determine chemical abundances in ionized nebulae, so the abundances derived from them should be reliable for the medium from which they arise.

Subject headings: cosmological parameters — Galaxies: abundances — ISM: abundances — ISM: kinematics and dynamics — planetary nebulae: NGC 7009

1. Introduction

Ionized gas is commonly used to determine chemical compositions and study the enrichment of heavy elements throughout the universe. To

convert the observed line intensities into ionic abundances, the electron temperature and density are normally required (e.g., Aller 1984; Osterbrock 1989). Traditionally, the line intensities used to measure the electron density and temperature as well as determine the chemical composition are collisionally-excited forbidden lines of common heavy elements (carbon, nitrogen, oxygen, neon, sulfur, and argon). Though challeng-

[†]deceased, 2012 Dec 26

¹Based on observations made with the European Southern Observatory telescopes obtained from the ESO/ST-ECF Science Archive Facility.

ing because they are weak, recombination lines may also be used to determine chemical abundances, as was first attempted by Wyse (1942). Invariably, the abundances derived from recombination lines are larger than those derived from collisionally-excited lines, at least for carbon, nitrogen, oxygen, and neon (Liu 2010), leading to what is known as the abundance discrepancy. Peimbert & Peimbert (2006), Liu (2006, 2010), and Bohigas (2009) provide recent reviews.

The ratio of abundances derived from optical recombination lines (ORLs) and collisionally-excited lines (CELs) is known as the abundance discrepancy factor (ADF). The ADF is found in both planetary nebulae and H II regions. García-Rojas & Esteban (2007) emphasize that the nature of the ADF is, possibly, different in H II regions, where it is almost always near a factor of two, and in planetary nebulae, where much larger values are encountered about 20% of the time. In both H II regions and planetary nebulae, the ADFs for carbon, nitrogen, oxygen, and neon tend to be similar for a given object, i.e., element ratios such as N/O are unaffected (e.g., Liu 2010).

Attempts to explain the ADF phenomenon have focused mainly upon the appropriate temperature to use when deriving abundances and the effects of deviations about some mean temperature. Peimbert (1967) first noted that the use of a single temperature derived from collisionally-excited forbidden lines was likely to overestimate the true mean temperature and underestimate the ionic abundances subsequently derived. Taking temperature fluctuations into account allows, in many cases, to reconcile the abundances derived from CELs and ORLs (e.g., Esteban et al. 2004). Liu et al. (2000), inspired by the unusually large ADF found for NGC 6153, argued that a second plasma component, consisting of cold, hydrogen-deficient clumps, embedded in the normal nebular material was a more natural explanation. Other ideas have been less explored, but include enhanced radiative or dielectronic recombination and departures of the electron energy distribution from the Maxwellian distribution (e.g., Garnett & Dinerstein 2001a; Rodríguez & García-Rojas 2010; Pradhan et al. 2011; Nicholls et al. 2012). Dust discs around the central stars are another possibility (Bilfková et al. 2012). Finally, detailed observations of the Orion

nebula indicate that density structures, such as proplyds or shocks, can distort the electron temperatures and densities derived from CELs if not taken into account (Mesa-Delgado et al. 2008, 2009a,b, 2012; Tsamis et al. 2011).

There are several means to determine the electron temperature in ionized plasmas (for details, see Aller 1984; Osterbrock 1989). The result's sensitivity to the underlying temperature and any variations will depend upon the ion used, the conditions in which it is found, and the means by which the transitions are excited. The most commonly-used temperatures are determined from CELs, the Balmer jump, and the ratio of ORLs. The intensity of CELs have an exponential dependence upon the electron temperature that characterizes the Maxwellian distribution of the kinetic energy of the free electrons. Since temperature measurements depend upon the ratio of two such lines, the result will also have an exponential dependence upon temperature. On the other hand, the intensity of ORLs usually have a power law dependence upon the temperature, $T^{-\beta}$ with typically $\beta \sim 1$. Ratios of ORLs will therefore have only a weak power law dependence upon the temperature. The Balmer jump depends upon temperature as $T^{-3/2}$, so the temperature, based upon the ratio of a Balmer line to the Balmer jump, has an approximately square root dependence upon temperature.

As might be expected as a result of the temperature structure in any given object, the different temperatures do not always agree. In general, the temperatures derived from CELs are the highest, followed by Balmer jump temperatures, and with temperatures derived from ORLs of neutral helium or ionized oxygen being the coldest (e.g., Liu 2010). Using hotter temperatures to derive chemical abundances from ORLs helps reconcile them with the abundances determined from CELs. Obviously, meaningful ionic abundances are obtained only if the electron temperature is appropriate for the emitting ions.

Much effort has been invested in searching for trends between the ADF and the nebular properties in the hope of uncovering the ADF's origin. In planetary nebulae, the ADF increases as the difference between the Balmer jump and [O III] $\lambda\lambda$ 4363,4959,5007 temperatures increases (Liu et al. 2001). Likewise, the ADF increases

in planetary nebulae that are larger, more diffuse, and of lower surface brightness, but not with expansion velocity, electron temperature, $\text{He}^{2+}/\text{He}^+$ ratio, or the stellar temperature or luminosity (Robertson-Tessi & Garnett 2005). The trends with size, density, and surface brightness could suggest that part of the ADF phenomenon in planetary nebulae has to do with the evolutionary stage. Tsamis et al. (2008) find trends with opposite signs between the electron temperature (CELs) and abundances of oxygen derived from ORLs and CELs, finding high recombination line abundances in regions that are more highly ionized and of higher electron temperature. In H II regions, there may be weak correlations between increasing ADF and an increasing difference between the Balmer jump and $[\text{O III}]\lambda\lambda 4363, 4959, 5007$ temperatures and with increasing excitation energy, but, within observational uncertainties, no correlation has been found with the abundance of oxygen or of doubly ionized oxygen, the ionization degree, nebular temperatures, the width of the hydrogen lines, or the effective temperature of the main ionizing stars (García-Rojas & Esteban 2007).

Here, we study NGC 7009, whose ADF is about 5 (Liu et al. 1995; Luo et al. 2001; Fang & Liu 2012). Rubin et al. (2002) attempted to observe the temperature fluctuations postulated by Peimbert (1967) using imaging and spectroscopy from the Hubble Space Telescope. This is a difficult endeavor, as any observation will necessarily average the temperature structure along the line of sight to some extent, even at high spectral resolution because of Doppler broadening and the consequent mixing from plasma at different positions (or velocities) cannot be avoided. Rubin et al. (2002) were unable to observe fluctuations as large as needed, but could not exclude the possibility that larger fluctuations existed and were averaged out.

Here, we present spatially- and velocity-resolved echelle spectroscopy for NGC 7009. In §2, we describe the data and the construction of the position-velocity maps. In §3, we use these maps to investigate the ionization structure of NGC 7009, the contribution of recombination to the $[\text{N II}]\lambda 5755$ emission, the component structure of $\text{C II } \lambda 4267$, and fluorescence in N II lines. In §4, we consider the location and possible origins of

the ORLs and its consequences for the abundance discrepancy. We present our conclusions in §5.

2. Observations and Construction of PV Diagrams

The data were retrieved from the ESO data archive from spectra obtained on 2002 Aug 4 using the UV-Visual Echelle Spectrograph (UVES) attached to the European Southern Observatory (ESO) Very Large Telescope (VLT) UT2/Kueyen 8.2m telescope as part of program ID 69.D-0413(A). Fig. 1 shows the two slit positions in NGC 7009 analyzed here. All of the data were acquired within a time span of one hour. The standard star observed was HR 9087 (program ID 60.A-9022(A)).

UVES is a two-armed, cross-dispersed echelle spectrograph installed on the Kueyen Nasmyth B platform. The blue arm uses a single EEV 44-82 2048×4096 CCD with $15 \mu\text{m}$ pixels while the red arm uses a mosaic of an EEV CCD (same model) and an MIT-LL CCID-20 2048×4096 CCD with $15 \mu\text{m}$ pixels. The data were obtained in the standard DIC1 mode with cross dispersers CD2 and CD3 in the blue and red arms, respectively, so the spectra cover the $3259\text{-}4518\text{\AA}$, $4584\text{-}5600\text{\AA}$, and $5655\text{-}6672\text{\AA}$ wavelength regions. A $1''.5$ wide slit was used for both the red and blue arms. The slit lengths were different, though, $8''.0$ for the blue arm and $11''.0$ for the red (Fig. 1). The resulting spectral resolution was approximately 33,000 in the blue, gauged by the width of arc lamp lines, and approximately 31,000 in the red, as gauged from the width of the telluric $[\text{O I}]\lambda 5577$ line. The plate scale was $0''.25/\text{pixel}$ and $0''.18/\text{pixel}$ in the blue and red arms, respectively. UVES's atmospheric dispersion corrector (ADC) was used in AUTO mode for all observations of NGC 7009, but was not used for the observation of HR 9087.

The data were reduced using the Image Reduction and Analysis Facility² (IRAF). We subtracted biases from all images. We traced the position of the standard star spectrum to determine the positions of the spectral orders. We normalized each order of the flat field image and inspected

²IRAF is distributed by the National Optical Astronomical Observatories, which is operated by the Associated Universities for Research in Astronomy, Inc., under contract to the National Science Foundation.

the resulting image for interference fringes or spatial variations at the wavelengths of the emission lines of interest. Since neither were found at the level of the noise, we decided not to apply the flat field correction to the data. We calibrated the wavelength scale using arc spectra taken the same night, whose internal precision is better than 1 km/s. We used the observation of the standard star to calculate the sensitivity function (including the correction for the blaze function). No correction was applied for reddening, since absolute line ratios will not be crucial to our analysis. We applied no heliocentric correction to the radial velocity.

We construct position-velocity (PV) maps (or diagrams) from our echelle spectra. In these diagrams (see Fig. 2), one axis corresponds to the spatial coordinate along the slit (the vertical direction in this case) while the other presents the velocity distribution of the emission at each spatial position. From PV diagrams such as Fig. 2, it is possible to infer which features seen in direct images are on one side or the other of the object and how others, such as the main shell, are coherent, large-scale spatial constructs that constitute the fundamental three-dimensional structure of the object.

To construct PV maps for each slit position, we used the spatial position of the standard star as our reference spatial position. We then extracted pixel-by-pixel strips parallel to the traced position of the standard star. These spatial strips were then calibrated in both wavelength and flux. We used IDL routines to resample all of the spectra to a common $0''.5$ spatial scale and to construct the PV arrays for each position observed in NGC 7009. In the few cases where it was necessary, cosmic rays were removed using IRAF's *imedit* task. Since the ADC was not used for the observations of HR 9087, we corrected for differential atmospheric refraction by mapping the position of NGC 7009's central star in slit position 1 as a function of wavelength to determine the spatial offset correction. This correction was applied to the PV arrays for both slit positions in NGC 7009. We removed the spectra of the central star and the nebular continuum from the PV arrays by interpolating the spatial profiles on both sides of the emission lines of interest.

Finally, the PV maps for the two slit positions

were merged into a single PV map by scaling the flux in the position 2 spectrum to that in the position 1 spectrum in the region of overlap. Since there is no overlap for the blue spectra, the flux scaling is based upon the red spectra only. The lack of overlap in the blue spectra produces an "interpolation gap" in the PV maps (see Fig. 2). Note that the [O III] $\lambda 4959$ line is saturated in the second slit position, which introduces artifacts when this PV diagram is compared to others. We have identified this region in the following figures when relevant.

We present PV diagrams for NGC 7009 in different emission lines in Fig. 3. The lines and the maximum intensity are identified at upper left in each panel. In all cases, the velocity range spans the range from -110 to +10 km/s and is not corrected for heliocentric motion. The horizontal line indicates the position of the central star and the spatial scale is given in seconds of arc. The instrumental broadening limits the spectral resolution for some kinematic components of some lines, such as the approaching wall of the main shell in the lines of [O III] $\lambda 4959$ and [Ar IV] $\lambda 4711$. For the hydrogen and helium lines thermal broadening and the fine structure (He I singlets excepted) further broadens the lines. For other lines, presumably the broadening is due to the kinematic structure. For all the lines shown in Fig. 3, the distribution of the emission on the receding side (redshifted) of the nebula is broadened beyond that due to instrumental broadening, presumably due to kinematic structure.

The main features in our PV diagrams are what Sabbadin et al. (2004) call the main shell and the SW cap (see Figs. 1 and 2). In Fig. 3, the main shell is prominent in higher ionization lines, such as He I $\lambda 4922$, [O III] $\lambda 4959$, [Ar IV] $\lambda 4740$, or He II $\lambda 4686$, but very faint in low ionization lines, such as [O II] $\lambda 3726$, and likely optically-thin due to the absence of [O I] $\lambda 6300$ (see also Sabbadin et al. 2004). The SW cap is seen best in the [N II] $\lambda 6583$ image (Fig. 2), where it appears as a bright filamentary structure running nearly perpendicular to the main shell, and is best seen in the [O II] $\lambda 3726$ and [O I] $\lambda 6300$ PV diagrams in Fig. 3. Its velocity and low level of ionization, indicate that it is outside the main shell (Sabbadin et al. 2004). The SW cap has very low mass since it is nearly absent in the $H\beta$ PV dia-

gram (Fig. 3), but it is the only direction covered by these observations that could be optically-thick to ionizing radiation (strong [O I] λ 6300).

Comparing PV diagrams quantitatively requires care, e.g., taking ratios to compute the physical conditions or to model one PV diagram as a sum of several others, since such comparisons require precise alignment in both the spatial and velocity axes. We avoid comparing the PV diagrams of lines with fine structure. Only occasionally must we compare lines with different thermal widths (and account for it). We require a physically-consistent wavelength scale that places co-spatial emission from different ions at the same radial velocity, while mitigating the effects of any errors due to our wavelength calibration or laboratory wavelength measurements. The assumptions involved should not introduce spurious kinematic structure. Our adopted wavelengths are given in Table 1, taken from Clegg et al. (1999) for H I and He II lines, Bowen (1960) for CELs, and from the NIST database (Ralchenko et al. 2011)³ for the remaining lines.

There are many studies of the structure and kinematics of NGC 7009 (e.g., Bohigas et al. 1994; Gonçalves et al. 2003; Sabbadin et al. 2004; Steffen et al. 2009; Phillips et al. 2010). Its kinematic structure appears reasonably simple, with homologous (radial) expansion dominating except perhaps towards the eastern and western extremities of the shell (Sabbadin et al. 2004; Steffen et al. 2009). These results suggest that the mean velocity of the middle section of the main shell may be constant for all ions. This should be true for lines from a given ion or lines from co-spatial ions. Whether this assumption is reasonable for lines that are not expected to arise co-spatially is unclear, e.g., He II λ 4686 and [O II] λ 3726,3729, but we are typically able to avoid comparing the PV diagrams of these line pairs. So, we align all PV diagrams in velocity by measuring the velocities of the blue- and red-shifted components in the middle section of the main shell and shifting the mean of these two velocities to a common mean velocity. We measure these velocities in the the spatial region from $+0''.5$ to $+2''.5$ SW of the central star (see Fig. 3), chosen to avoid the central star, but still very central in

order to suffer little from projection effects due to the geometry of nebular shell. We adopt the mean velocity for the sum of the O II λ 4639,4649 lines as the common mean velocity. Note that measurements of *line splitting* are unaffected by the velocity alignment of the PV diagrams.

3. Results

3.1. Ionization structure

Table 1 confirms the simple structure of NGC 7009's main shell. The last column presents the total velocity splitting between the main shell components for the spatial region from $+0''.5$ to $+2''.5$ SW of the central star. We determined the total velocity splitting by fitting a single Gaussian to the velocity component for the front and back walls of the main shell. Most of the lines in Table 1 are isolated at the resolution of our observations. Fig. 4 presents a section of spectrum spanning the O II λ 4639,4642,4649,4651 lines that are usually blended with the N III λ 4641,4642 Bowen fluorescence lines and the C III λ 4647,4650,4651 recombination lines at lower resolution (cf. Fang & Liu 2011). Clearly, at our resolution, the O II λ 4639,4649 recombination lines are free of blending. Of the other lines in Table 1, N III λ 4379 is perhaps contaminated by Ne II λ 4379 (13% level), He I λ 4922 may be contaminated by [Fe III] λ 4922 (10% level), while C II λ 4267 and [N II] λ 6583 may be contaminated at the 1% level (Fang & Liu 2011). We disregard contamination below 1%.

There is clear ionization stratification within the main shell (e.g., Wilson 1950, Table 1, Fig. 3). The lines expected to be emitted from the bulk of the main shell's volume, the H Balmer lines, He I λ 4922, and [O III] λ 4959 have a velocity splitting of 39-40 km/s. The lines from the most highly ionized ions, He II λ 4686, N III λ 4379, and O III λ 3707, have the smallest velocity splitting at 33-34 km/s. At an intermediate velocity splitting, about 36 km/s, we find C II λ 6578, O II λ 4639,4649, and [Ar IV] λ 4711,4740. The largest velocity splitting, about 41 km/s, occurs for [N II] λ 6583 and [O II] λ 3726,3729. We note that the velocity splitting for [N II] λ 5755 and [O III] λ 4363 differs from that for [N II] λ 6548 and [O III] λ 4959, respectively. Thus, within each wall of the main shell, the average velocity of the high-

³<http://physics.nist.gov/asd>

est ionization species differs from that of the lowest ionization species by only about 4 km/s. The main shell does not emit in [O I] over the area surveyed here, so we conclude that it is optically thin to hydrogen ionizing radiation over this area.

The lines with intermediate velocity splitting of about 35-37 km/s divide into two groups. One group is from ions expected in the region where He^{2+} recombines to He^+ , i.e., [Ar IV] $\lambda\lambda 4711, 4740$, the Bowen lines of O III $\lambda 3444$ and N III $\lambda 4641$ excited by He II Ly α in the innermost part of the O^{2+} zone, and lines excited by the $\text{O}^{3+} + \text{H}^{\circ} \rightarrow \text{O}^{2+} + \text{H}^+$ charge exchange reaction. Ionization stratification should locate this emission naturally at velocities between those of He II $\lambda 4686$ and [O III] $\lambda 4959$. The second group, recombination lines of C II, N II, O II, and Ne II, is not expected where He^{2+} recombines to He^+ , but where doubly ionized ions of these elements are most common within the $\text{O}^{2+}/\text{Ne}^{2+}$ zone, and so with a velocity splitting similar to [O III] $\lambda 4959$ and [Ne III] $\lambda 3869$.

Our data sample the ionization structure of oxygen in NGC 7009 particularly well. The O III $\lambda 3707$ recombination line samples the O^{3+} zone, the O III $\lambda\lambda 3444, 3757, 5592$ lines sample the transition zone between O^{3+} and O^{2+} via both Bowen fluorescence and charge transfer, the [O III] $\lambda\lambda 4363, 4959$ and O II $\lambda\lambda 4639, 4949$ lines sample the O^{2+} zone in collisionally-excited and recombination lines, the [O II] $\lambda\lambda 3726, 3729$ lines sample the O^+ zone, and the [O I] $\lambda 6300$ line samples the transition zone where both oxygen and hydrogen recombine to neutral atoms. (The PV diagrams for O III $\lambda\lambda 3757, 5592$ are statistically indistinguishable from that for O III $\lambda 3444$, but of considerably lower signal-to-noise.) The kinematics are expected to reflect the ionization structure, with the innermost zones showing the smallest line splitting and the outermost zones suffering the greatest splitting. This expectation is borne out (Table 1), but for the anomaly already noted, that the velocity-splitting of the O II recombination lines is smaller than that for the [O III] $\lambda 4959$ line.

Other ions confirm the ionization structure inferred from oxygen: N III $\lambda 4379$ coincides with O III $\lambda 3707$, [Ne III] $\lambda 3869$ coincides with [O III] $\lambda 4959$, and [N II] $\lambda 6583$ coincides with [O II] $\lambda\lambda 3726, 3729$. Comparing the PV diagrams for

[O III] $\lambda 4959$ and [O II] $\lambda 3726$ differentially with respect to He I $\lambda\lambda 4922, 5016, 5876$ and He II $\lambda 4686$, we find the expected differences, given the differences in ionization potentials: [O II] $\lambda 3726$ traces material outside the He^+ zone, but also includes the outermost material, in both velocity and spatial extent, traced by He^+ . [O III] $\lambda 4959$ generally follows the He^+ distribution, but also shows emission at the positions and velocities where the He II $\lambda 4686$ emission is enhanced, reflecting the O^{2+} ions in the outermost part of the He^{2+} zone. Therefore, the ionization structure of oxygen, as traced by O III $\lambda 3707$, Bowen and charge exchange emission, [O III] $\lambda 4959$, [O II] $\lambda 3726$, and [O I] $\lambda 6300$, appears secure. This structure is also that predicted by hydrodynamic models of planetary nebulae at NGC 7009's stage of evolution (e.g., Villaver et al. 2002; Perinotto et al. 2004).

On the other hand, the anomaly of the O II lines is not isolated. The recombination lines of C II, N II, and Ne II have a line splitting similar to that of the O II recombination lines. Therefore, all of these recombination lines have velocity splittings that are smaller than expected.

3.2. Physical conditions and [N II] $\lambda 5755$ recombination

Fig. 5 presents PV diagrams for the physical conditions of electron temperature and density. To compute these PV diagrams, it is necessary to take the ratio of two PV diagrams, e.g., [O III] $\lambda 4363$ and [O III] $\lambda 4959$ to compute the [O III] temperature or [Ar IV] $\lambda 4711$ and [Ar IV] $\lambda 4740$ to compute the [Ar IV] density. In the case of the [O III] and [N II] temperatures, we converted the [O III] $\lambda\lambda 4363, 4959$ and [N II] $\lambda\lambda 5755, 6584$ line ratios to electron temperatures using equations 5.4 and 5.5, respectively, from Osterbrock (1989), assuming an electron density of 4000 cm^{-3} and the atomic data used therein (Nussbaumer & Rusca 1979; Nussbaumer & Storey 1981). For the [O II] and [Ar IV] density maps, we converted the [O II] $\lambda\lambda 3726, 3729$ and [Ar IV] $\lambda\lambda 4711, 4740$ line ratios to electron density using the atomic data incorporated into the STSDAS version 3.8 nebular package, assuming an electron temperature of 10,000 K (Bowen 1960; Kaufman & Sugar 1986; Zeppen et al. 1987; McLaughlin & Bell 1993; Wiese et al. 1996).

The density distribution agrees with previous

findings, e.g., Sabbadin et al. (2004) with which we can compare most easily. The electron density in the main shell is rather uniform based upon the [Ar IV] lines, with values typically of $\sim 6000 \text{ cm}^{-3}$. The only exception is a dense filament crossing the approaching face of the main shell, seen clearly in the HST images (Fig. 2) and the PV diagrams for $\text{H}\beta$, He I $\lambda 4922$, [O III] $\lambda 4959$ and [Ne III] $\lambda 3869$ (Fig. 3). Since this filament is fainter in He II $\lambda 4686$, O III $\lambda 3444$, and [N II] $\lambda 6583$ (Figs. 2, 3 and 6) than in [O III] $\lambda 4959$, it is presumably located midway through the main shell structure. The SW cap is less dense, $\sim 2000 \text{ cm}^{-3}$ as judged from the [O II] lines. The lower density makes sense given its near-absence in the $\text{H}\beta$ PV diagram (Fig. 3).

The electron temperature found in the outer (SW) part of the nebula (upper part of the PV diagrams) fluctuates around a value of 10^4 K , with good agreement between the temperatures from the [O III] and [N II] lines. As expected, the temperature is lower in the filament (Fig. 2) where the density is higher. Both the [O III] and [N II] lines indicate that the regions nearer the central star are hotter, but the variation implied by the [N II] lines is much greater, up to values exceeding $2 \times 10^4 \text{ K}$. While we do not have the signal-to-noise to construct a PV diagram for the [Ne III] temperature, we can calculate its value in the main shell components near the central star (the same region used to measure the kinematics in Table 1, $0''.5\text{--}2''.5$ SW of the central star). We find [Ne III] $\lambda 3869$ /[Ne III] $\lambda 3342$ ratios of 573 and 556 in the blue- and red-shifted components of the main shell, respectively. These ratios imply temperatures of 10750 K and 10840 K for the blue- and red-shifted components, respectively, and confirm the temperature found from the [O III] lines in this region, precisely where the [N II] temperature is anomalous.

Important differences between the [N II] and [O III] temperatures have been found previously in NGC 7009 (e.g., Liu & Danziger 1993; Liu et al. 1995; Fang & Liu 2012) and have been attributed to a recombination contribution to [N II] $\lambda 5755$ (Liu et al. 2000). In Fig. 6, we compare the [N II] $\lambda\lambda 5755, 6583$ PV diagrams (top row). Clearly, there are additional emission components in the [N II] $\lambda 5755$ map. These could arise via collisional excitation if the regions of excess [N II] $\lambda 5755$ emission were either very hot or very dense. If

these regions were very hot, they should be even more prominent in [O III] $\lambda 4363$ and they are not (Fig. 3). If these regions were very dense, this should be evident from the ratio of the [Ar IV] $\lambda\lambda 4711, 4740$ or [O II] $\lambda\lambda 3726, 3729$ lines, if they are ionized, or from the presence of [O I] $\lambda 6300$ if they are neutral, but the [Ar IV] and [O II] densities are not unusual and [O I] $\lambda 6300$ is absent, so high density can also be ruled out (Figs. 3 and 6). Therefore, the excess [N II] $\lambda 5755$ emission is presumably not the result of collisional excitation.

If the additional components in [N II] $\lambda 5755$ are due to recombination, it should be possible to model this map as a linear superposition of the [N II] $\lambda 6583$ map and a recombination line map, such as O II $\lambda\lambda 4639, 4649$. (Such a decomposition implicitly assumes a constant electron temperature in the N^+ zone.) In Fig. 6, we present a model [N II] $\lambda 5755$ map (second row, right) and it is very similar to the observed [N II] $\lambda 5755$ map, as the difference of the two reveals (third row, right). (The intercept of the fit was forced through the origin, equivalent to supposing that the continuum emission in all PV diagrams is zero.) If we subtract the model [N II] $\lambda 6583$ component from the observed [N II] $\lambda 5755$ map, we obtain the “[N II] $\lambda 5755$ excess” map (second row, left). The map of the excess [N II] $\lambda 5755$ emission is very similar to the O II $\lambda\lambda 4639, 4649$ PV diagram (third row, left; see Fig. 7 for more examples of PV diagrams of recombination lines), which suggests that this excess emission is indeed due to recombination (c.f. Liu et al. 2000).

We can use this decomposition to compute the [N II] temperature, approximately correcting for the recombination contribution to [N II] $\lambda 5755$. At bottom right in Fig. 6, we present the [N II] temperature map computed after subtracting the model O II $\lambda\lambda 4639, 4649$ emission component from the observed [N II] $\lambda 5755$ PV diagram. This [N II] temperature map is now similar to the [O III] temperature map in Fig. 5, though of much lower signal-to-noise near the central star.

The agreement of the temperatures calculated from the lines of [O III], [Ne III], and [N II] (corrected for the recombination contribution to [N II] $\lambda 5755$) implies that the quality of the atomic data for these collisional transitions is reasonable. Therefore, we conclude that recombination excitation of the [N II] $\lambda 5755$ line

(Nussbaumer & Storey 1984) is the most plausible explanation for the difference in the [O III] and [N II] temperature maps, as has been argued previously for NGC 7009 and other planetary nebulae (Liu et al. 2000; Tsamis et al. 2003; Wesson et al. 2005).

In theory, recombination should excite both the auroral and nebular lines of N^+ and O^+ (Nussbaumer & Storey 1984). However, the recombination contribution to the intensities for auroral and nebular lines are similar while the collisional contribution to the nebular lines is 1-2 orders of magnitude larger (Liu et al. 2000). The difference between the PV diagrams of [N II] $\lambda 6583$ and [O II] $\lambda 3726$ compared to that of O II $\lambda\lambda 4639, 4649$ (Figs. 3 and 6) illustrate this clearly for NGC 7009. Therefore, the recombination contribution to the nebular lines can be ignored in NGC7009 (and probably most other PNe).

The line splitting also differs between [O III] $\lambda 4363$ and [O III] $\lambda 4959$ (Table 1). In this case, however, the PV diagrams have very similar morphologies (Fig. 3). In addition, the [O III] $\lambda 4363$ PV diagram has no components in common with the PV diagram for O III $\lambda 3707$ that results from recombination of O^{3+} , as expected since the quantity of O^{3+} available to recombine is very small outside the innermost part of the O^{2+} zone (see Fig. 9). (N^{2+} recombination to [N II] $\lambda 5755$ is much more relevant because there is much more N^{2+} than N^+ ; Fig. 9.)

The O^{2+} ion is the most efficient coolant available in most planetary nebulae. So, it is natural that the temperature rise where O^{2+} is not the dominant ionization state of oxygen, as occurs in the He^{2+} zone where the fraction of O^{3+} begins to increase. It is therefore also natural that the [O III] $\lambda 4363$ emission is slightly biased to the inner regions of the O^{2+} zone. Similarly, in the SW cap, there is a slight increase in the [N II] (and [O III]) temperature where the [O I] $\lambda 6300$ emission peaks (Fig. 5), presumably indicating the position of a transition zone and the loss of N^+ as an important coolant.

3.3. C II $\lambda 4267$

In Fig. 7, we present more PV diagrams for recombination lines of C II, N II, O II, and Ne II. Their similarity is notable in both the positions

and velocities of the four main emission components, the two peaks in both the red- and blue-shifted components. With the exception of the C II $\lambda 6578$ line, the relative intensities of these components are maintained. Note that, in addition to recombination, fluorescence may contribute indirectly to the excitation of C II $\lambda 6578$ and N II $\lambda 5680$, i.e., fluorescence can excite levels that can then decay to the upper level of these transitions (Grandi 1976; Sharpee et al. 2004). The decomposition of the [N II] $\lambda 5755$ line has already been discussed (§3.2).

The C II $\lambda 4267$ PV diagram is surprising (Fig. 7). It appears to be composed of only two emission components, not the three expected, i.e., (NIST; Atomic Line List v. 2.05b16/P. van Hoof⁴). Presumably, we do not detect the $2s^2 4f^2 F_{5/2}^o$ to $2s^2 3d^2 D_{5/2}$ transition, the weakest and reddest component. Also, the separation between the two components we observe, the $2s^2 4f^2 F_{7/2}^o$ to $2s^2 3d^2 D_{5/2}$ and $2s^2 4f^2 F_{5/2}^o$ to $2s^2 3d^2 D_{3/2}$ transitions, is 0.222\AA (15.6 km/s) rather than the 0.182\AA or 0.260\AA expected (NIST; Atomic Line List v. 2.05b16/P. van Hoof⁴).

We have isolated the red emission component (Fig. 7, second row, left panel), nominally at $4267.183/4267.261\text{\AA}$, by modeling the C II $\lambda 4267$ PV diagram as a linear superposition of two O II $\lambda\lambda 4639, 4649$ PV diagrams that are shifted in velocity. The PV diagram for the red component is obtained by subtracting the blue component from the original C II $\lambda 4267$ PV diagram. (As before, the intercept of the fit was forced through the origin.)

3.4. N II fluorescence lines

Several N II multiplets may be excited by fluorescence from starlight or He I $\lambda 508.64$ (e.g., Grandi 1976; Sharpee et al. 2004). As already noted, N II $\lambda 5680$ and other lines of its multiplet (V3) can result from the de-excitation of the lines from multiplet V30 (N II $\lambda\lambda 3829.80, 3842.19, 3855.10$) that are strongly affected by resonance fluorescence from He I $\lambda 508.64$, as can multiplet V5, of which N II $\lambda 4630.54$ is the strongest component. Resonance fluorescence by starlight can excite multiplets V20, V21, V24, V28, and V29, of which the strongest lines are N II $\lambda 4994.37$

⁴<http://www.pa.uky.edu/~peter/newpage/>

(V24) and N II $\lambda\lambda 5931.79, 5941.65$ (V28). Only N II $\lambda\lambda 4631, 5932, 5942$ have sufficient signal to construct (noisy) PV diagrams (as well as N II $\lambda 5680$ and other lines from multiplet V3).

If these lines are excited purely by recombination, their PV diagrams should appear similar to other recombination lines, such as O II $\lambda\lambda 4639, 4649$. If they result purely from fluorescence, their PV diagrams should be more similar to the PV diagram of [N II] $\lambda 6583$. Fig. 8 presents the PV diagrams for the strongest of the N II fluorescence lines in our data, N II $\lambda\lambda 4631, 5932, 5942$ as well as [N II] $\lambda 6583$ and O II $\lambda\lambda 4639, 4649$. (N II $\lambda 5680$ appears in Fig. 7.) Like the N II $\lambda 5680$ PV diagram, those for N II $\lambda\lambda 4631, 5932, 5942$, though noisy, are more similar to the PV diagrams of recombination lines than to that for [N II] $\lambda 6583$. We conclude that, in NGC 7009, these lines are excited overwhelmingly via recombination, confirming the opinion of Sharpee et al. (2004) that different excitation mechanisms have different effects in different objects.

4. Discussion

4.1. Modeling the ionization structure

To provide context for the results of §3.1, we present the ionization structure for generic model nebulae in Figs. 9 and 10. Both figures present the fractional ionization as a function of distance from the ionizing source. The figure captions provide details concerning the model parameters. The models in Fig. 9 and the second panel of Fig. 10 contain the ionizing sources most likely to be similar to the central star in NGC 7009. The ionization structure of these two models is very similar to that deduced from the kinematics of NGC 7009: The dominant ions throughout the bulk of the main shell, especially if it is optically thin, are H^+ , He^+ , O^{2+} , and Ne^{2+} . The $O^{3+} \rightarrow O^{2+}$ transition zone occurs within the He^{2+} zone and more or less coincides with the Ar^{3+} zone.

In all cases, the zones where C^{2+} , N^{2+} , O^{2+} , and Ne^{2+} are the dominant ions of these elements coincide rather closely. The C II, N II, O II, and Ne II recombination lines should arise primarily where these doubly-ionized ions recombine to the singly ionized state, i.e., where the singly-ionized stage of these elements is the *second* most abundant stage (see the arrows in Fig. 9). For the mod-

els with a significant He^{2+} zone, as in NGC 7009, the zone where C^+ and N^+ are the second most abundant stage differs significantly from the zone where O^+ and Ne^+ are the second most abundant stage, since the C^{3+} and N^{3+} zones extend deeply into the C^{2+} and N^{2+} zones, respectively. Therefore, these models predict different kinematics for C II and N II lines, in particular a larger velocity splitting, compared to O II and Ne II lines. In contrast, we observe similar kinematics for all of these lines in NGC 7009.

In reality, this problem may not be so acute, because NGC 7009's main shell is optically thin to ionizing radiation. As a result, the models in Fig. 9 and the top three panels of Fig. 10 should be truncated prior to the $H^+ \rightarrow H^0$ transition zone. Depending upon where the models are truncated, the C II and N II lines should be significantly weaker than expected due to ionization equilibrium, but would allow the zones emitting the C II, N II, O II, and Ne II recombination lines to coincide more closely, perhaps explaining their similar kinematics.

On the other hand, truncating the models as described is problematic as regards the abundances derived from the C II, N II, O II, and Ne II lines. From the truncated models, lower C^{2+} and N^{2+} abundances would be expected as compared to the O^{2+} and Ne^{2+} abundances, since a large fraction of the C^{2+} and N^{2+} zones is excluded. Yet, the over-abundance of C^{2+} , N^{2+} , O^{2+} , and Ne^{2+} derived from recombination lines in NGC 7009 are similar (Liu et al. 1995; Luo & Liu 2003; Fang & Liu 2012).

So, the models in Fig. 9 and the top three panels of Fig. 10 are not simultaneously compatible with the kinematics and chemical abundances from recombination lines in NGC 7009. To be compatible with the kinematics we observe, the models should be truncated. If they are truncated, the models should be incompatible with the ionic over-abundances derived from the C II, N II, O II, and Ne II lines (Liu et al. 1995; Luo & Liu 2003; Fang & Liu 2012).

4.2. Location of the ions emitting C II, N II, O II, and Ne II lines

The O^{2+} ion is responsible for four PV diagrams in Fig. 3, the collisionally-excited [O III]

$\lambda\lambda 4363, 4959$ lines, the O III $\lambda 3444$ Bowen fluorescence line, and the O II $\lambda\lambda 4639, 4649$ recombination lines (also Table 1). The structure of the PV diagram of the O III $\lambda 3444$ Bowen fluorescence line is notably different from that of the [O III] $\lambda\lambda 4363, 4959$ or O II $\lambda\lambda 4639, 4649$, but resembles that for He II $\lambda 4686$ in that the “loop” at the top/SW of the diagram is replaced by a broad, detached kinematic component that shows little spatial structure.

The Bowen and collisionally-excited lines are expected to differ since the spatial volumes in which they are excited differ. The PV diagrams differ in the sense expected, since the Bowen lines should arise in the innermost part of the O^{2+} zone that overlaps the He^{2+} zone. Indeed, both the structure of the PV diagram of the O III $\lambda 3444$ line and its line splitting are similar to those of the He II $\lambda 4686$ line, as expected.

The structure of the PV diagrams for the [O III] $\lambda\lambda 4363, 4959$ collisional lines are very similar. However, their line splitting differs (Table 1). This difference was addressed in §§3.1 and 3.2 and can be understood in terms of the ionization and temperature structure of the nebula (§4.1).

That the PV diagrams for [O III] $\lambda 4959$ and O II $\lambda\lambda 4639, 4649$ differ is very important. In the absence of strong temperature gradients, ionization equilibrium in a chemically-homogeneous medium should impose similar position and velocity distributions on the collisional and recombination emission from O^{2+} (§§3.1 and 4.1; Figs. 9 and 10). Since the emissivity of recombination and collisionally-excited lines depend upon the temperature in opposite ways, the former decreasing and the latter increasing as the temperature increases, a temperature gradient could enhance the O II $\lambda\lambda 4639, 4649$ recombination emission from the coolest regions in a chemically-uniform plasma.

The top panel in Fig. 11 presents the PV diagram of the ratio of the emission in O II $\lambda\lambda 4639, 4649$ relative to that in the [O III] $\lambda 4959$ line. If the O II $\lambda\lambda 4639, 4649$ emission arose only from recombination of O^{2+} ions throughout the zone that emits [O III] $\lambda 4959$, the ratio should be constant in the outer part of the nebula and decrease in the inner part of the O^{2+} zone where the temperature increases (bottom panel in Fig. 11; also Fig. 5). While a gradient is seen, it is in the wrong sense, for it increases towards the innermost

part of the zone emitting [O III] $\lambda 4959$ where the temperature increases, rather than decreasing as expected.

The second and third panels of Fig. 11 present the PV diagrams of the ratios of O III $\lambda 3444$ and [Ar IV] $\lambda 4740$ relative to [O III] $\lambda 4959$. These two line ratios vary in a similar way as the ratio of O II $\lambda\lambda 4629, 4649$ to [O III] $\lambda 4959$. However, both the Ar^{3+} zone and the O III $\lambda 3444$ Bowen fluorescence are biased to the innermost part of the O^{2+} zone within the He^{2+} zone (Fig. 9), so their line ratios relative to [O III] $\lambda 4959$ vary as expected and confirm that the excess O II $\lambda\lambda 4629, 4649$ in the inner part of the O^{2+} zone is anomalous.

The structure of the top two panels in Fig. 11 differ in an important way. Clearly, the O III $\lambda 3444$ Bowen fluorescence (second panel) is much more restricted to the inner part (in velocity) of the O^{2+} zone than the emission from O II $\lambda\lambda 4639, 4649$ (top panel). This is especially apparent considering the velocity-space range occupied by the SW cap (Figs. 2 and 3). Thus, there is emission from O II $\lambda\lambda 4639, 4649$ from the entire zone from which the [O III] $\lambda 4959$ emission arises, but this is not the case for the emission from O III $\lambda 3444$. Therefore, the entire volume emitting in the [O III] $\lambda 4959$ forbidden line emits some O II $\lambda\lambda 4639, 4649$ recombination emission, as expected. What is unexpected is the additional emission from O II $\lambda\lambda 4639, 4649$ in the inner part of the O^{2+} zone. Given what is known of the temperature structure in NGC 7009 and the expectations of ionization equilibrium, the O II $\lambda\lambda 4639, 4649$ emission clearly does not trace the emission from [O III] $\lambda 4959$ in the inner part of the O^{2+} zone. Thus, there appear to be two emission components for the O II $\lambda\lambda 4639, 4649$ recombination lines in NGC 7009: one probably follows the [O III] $\lambda 4959$ emission throughout the O^{2+} zone as expected while the second is located near the $O^{3+} \rightarrow O^{2+}$ transition zone.

Our data (Table 1, Figs. 3 and 7) lead us to identical conclusions concerning the Ne II recombination lines and the collisionally-excited [Ne III] lines in NGC 7009. Although we lack CELs to trace the C^{2+} and N^{2+} zones, the models presented in §4.1 imply that the same would also be true for the C II and N II recombination lines.

There are few studies of the kinematics of the C II, N II, O II, and Ne II lines. Otsuka et al.

(2010, using an ADC) also found smaller expansion velocities from O II that were discrepant with the expectations of ionization equilibrium in the planetary nebula BoBn 1 ($ADF \sim 2 - 3$). On the other hand, the kinematics of the C II, N II, and Ne II lines was not discrepant. For DdDm 1 ($ADF \sim 12$), Otsuka et al. (2009) find that the kinematics of the N II and O II lines is compatible with the ionization structure derived from CELs. The results of Sharpee et al. (2004, IC 418) and Barlow et al. (2006, NGC 6153 and NGC 7009) are more difficult to interpret, since they were made without an ADC and on the bright rims of these objects, which cannot guarantee co-spatial observations at different wavelengths (e.g., Filippenko 1982) and can confuse ionization structure with projection effects, respectively. Only for NGC 6153 ($ADF \sim 9$) does the expansion velocity of O II $\lambda 4649$ appear to be smaller than that for [O III] $\lambda 5007$ (Barlow et al. 2006).

On the other hand, differences between the spatial distributions of CELs and ORLs of carbon and oxygen are well-known. Liu et al. (2000), Garnett & Dinerstein (2001a), Luo & Liu (2003), and Tsamis et al. (2008) find that the spatial profile of the O II recombination lines is more centrally-concentrated than that for the forbidden [O III] emission in NGC 6153, NGC 7009, NGC 6720, and (marginally) NGC 5882. Barker (1982, 1991) noted a similar effect for C II $\lambda 4267$ compared to C III] $\lambda \lambda 1906, 1909$ in NGC 6720 and NGC 2392. Supposing spherical or cylindrical symmetry, these differences in spatial profiles are compatible with the differences in kinematics we observe in NGC 7009.

We may therefore infer that the distributions of recombination and collisionally-excited lines through NGC 7009 differ, both *projected in the plane of the sky* and *along the line of sight*. Physically, one component of the O II $\lambda \lambda 4639, 4649$ recombination emission arises closer to the central star than does the majority of the collisionally-excited emission, i.e., the kinematics of this component of the O II $\lambda \lambda 4639, 4649$ recombination lines are like those of higher stages of ionization in NGC 7009. Given the similarity of their kinematics, the same is true for the C II, N II, and Ne II emission. Therefore, there is presumably the same additional emission component for all of these recombination lines and the volume from

which it arises is *not* the same volume as that from which collisionally-excited lines from the parent ions are emitted, as traced by [O III] $\lambda 4959$ and [Ne III] $\lambda 3869$. While we cannot say whether these volumes are mutually exclusive (§4.3), they are clearly well-mixed in the inner part of the O²⁺ zone (Fig. 11).

4.3. Cold clumps?

To detect cold clumps kinematically requires sufficient spectral resolution to at least resolve the thermal widths of the normal nebular plasma (emitting in CELs, resolution $> 10^5$) and demonstrate that the ORLs have narrower line widths. Our spectral resolution prevents this. However, even very high spectral resolution could be foiled if there are multiple clumps of the cold and normal plasmas at different velocities along the line of sight.

A less direct method for inferring the presence of two plasma components, one emitting the ORLs, the other the CELs, is to search for strong, local enhancements in the ratio of ORL to CEL emission. This can be done easily with the ratio of two PV diagrams. Again, very high spectral resolution is advantageous, especially if there are multiple clumps of the different plasma components along the line of sight. Our observations (Fig. 11) do not reveal spectrally resolved enhancements of O II $\lambda \lambda 4639, 4649$ relative to [O III] $\lambda 4959$, but a clear gradient, as already discussed. Thus, either (1) our spectral resolution smears both the ORL and CEL emission too much, (2) there are multiple clumps of the ORL- and CEL-emitting plasma components along all of our lines of sight through NGC 7009, or (3) the ORL-emitting plasma is widely distributed within the normal nebular plasma.

The fourth panel in Fig. 11 clearly shows that the He I $\lambda 4922$ emission does not have the spatial and velocity distribution of the O II $\lambda \lambda 4639, 4649$ emission. In spite of the poorer velocity resolution (the [O III] $\lambda 4959$ PV diagram was broadened to match the thermal width of the He I $\lambda 4922$ line), it is clear that the He I $\lambda 4922$ line emission closely follows that from [O III] $\lambda 4959$, as expected (Figs. 9 and 10). Clearly, the plasma component emitting the C II, N II, O II, and Ne II lines in the inner part of the O²⁺ zone does not emit particularly strongly in He I $\lambda 4922$. Hence, our observations

can only support a metal-rich plasma component emitting the C II, N II, O II, and Ne II lines in the inner part of the O²⁺ zone.

So, we find no clear evidence of chemically-distinct plasma components, such as cold, hydrogen-deficient clumps in NGC 7009 (e.g., Liu et al. 2000), but we cannot rule them out. In principle, they could give rise to the observed recombination lines at the locations and velocities observed (or anywhere, since there is no accepted explanation for their origin). If they were considerably more dense than the “normal” nebular plasma (allowing pressure equilibrium), they would naturally be of lower ionization degree, which would resolve the problem of coincident emission from C II, N II, O II, and Ne II (§4.1). The dense model in the bottom panel of Fig. 10 would not be spatially resolved at the distance of NGC 7009.

The hypothesis of dense clumps, however, is incompatible with the physical conditions derived from the N II and O II lines in NGC 7009 by Fang & Liu (2011) and Fang & Liu (2012). They find that both the temperature and density derived for these lines is *lower* than those derived for CELs. If true, the volume emitting these lines is not in pressure equilibrium with the volume emitting the CELs. We note that the atomic data that these authors used for O II has not been published.

4.4. Other options?

The [O III] temperature map in Fig. 5 clearly shows that measurable, large-scale temperature gradients exist within NGC 7009. Small-scale temperature fluctuations may also exist, but our spectral resolution limits our ability to measure their true amplitude. However, it is not evident that these temperature fluctuations could be responsible for the enhanced O II $\lambda\lambda 4639, 4649$ emission. Our observations, like those of Tsamis et al. (2008), find that the C II, N II/[N II], O II, and Ne II recombination emission coincides with regions of higher electron temperature, not lower temperatures, contrary to expectations if temperature fluctuations are responsible for enhancing the recombination lines.

The transition zones of triply to doubly ionized C, N, O, and Ne coincide with the region from which recombination lines of C II, N II, O II, and

Ne II originate in NGC 7009. Might the resulting doubly ionized ions somehow recombine efficiently to the singly ionized state? Even if this were feasible in NGC 7009, it could not be a general process because other planetary nebulae with large ADFs, such as DdDm 1 or NGC 40 (Liu et al. 2004; Wesson et al. 2005; Otsuka et al. 2009), do not possess triply ionized zones of C, N, O, and Ne.

Physical processes that affect recombination throughout the O²⁺ zone do not appear promising as an explanation for the kinematics of the C II, N II, O II, and Ne II lines in NGC 7009. Although dielectronic recombination could strongly enhance recombination lines where the temperature increases, as we observe, we would require similar enhancements for four ions with different electronic structures, which seems improbable. Fluorescence would require efficiently exciting minority ions (§3.1) and at least the N II lines in NGC 7009 do not appear to be excited primarily by fluorescence (§3.4). Rodríguez & García-Rojas (2010) and Pradhan et al. (2011) suggest that recombination coefficients could explain the differences between ORL and CEL abundances. While this might address a general effect, such as the typical ADF ~ 2 , it cannot explain our kinematics since it should enhance recombination throughout the region where doubly ionized C, N, O, and Ne are present and, like dielectronic recombination, would have to change in a similar way for four different ions. Likewise, the possibility of departures of the electron energy distribution from a Maxwellian distribution should affect the entire zone where doubly ionized C, N, O, and Ne are present (Nicholls et al. 2012). Again, such an effect might explain a general discrepancy (e.g., ADF ~ 2), but it would not produce the component of the C II, N II, O II, and Ne II emission we observe at the velocity of the O³⁺ \rightarrow O²⁺ transition zone in NGC 7009.

4.5. The abundance discrepancy

Given that there appear to be at least two O II emission components in NGC 7009 and that one does not arise from the same volume as the [O III] emission (§§4.2 and 4.3), it is clear that care must be taken to compare and interpret the chemical abundances derived from each type of line. In particular, it is indispensable to know the physical conditions under which each type of line emits.

Thus far, this type of analysis is not common, but Liu et al. (2006) have undertaken such an analysis for the planetary nebula Hf 2-2. Under the usual assumptions, Hf 2-2 has an ADF of 72 (the highest known), but, when appropriate temperatures and densities are assumed for the O II, [O III], and Balmer lines, comparable masses of O^{2+} are found from CELs and ORLs. Presumably, in other objects with smaller ADFs, the mass of O^{2+} implied by the O II lines is less.

Since one component of the O II emission arises from a different volume from that giving rise to the [O III] emission in NGC 7009, both must be measured to obtain the oxygen abundance for these plasma components. Since the component responsible for the O II lines also appears to give rise to the C II, N II, and Ne II lines, the same is presumably true for the carbon, nitrogen, and neon abundances. If the O II and [O III] lines arise from different plasma components, the meaning of the abundance “discrepancy” changes: It is no longer that the collisional and recombination lines imply abundances that disagree, but that they probe the chemical abundances in different plasma components and that the different plasma components have different chemical compositions. In NGC 7009, it is not a matter that one abundance is correct and the other wrong, as is commonly argued, but that they measure the oxygen abundance in different volumes within the object.

If there are multiple plasma components, it is important to understand the origin of each component in order to interpret the abundances derived for each of them. The standard analysis of nebular gas assumes a common origin for all of the material, the progenitor star in the case of planetary nebulae. This standard analysis will be reasonable in many cases, but not all. When there are multiple plasma components, it is not necessarily obvious that all have a common origin, especially when even their coexistence is not understood. Furthermore, depending upon the astrophysical interest in the chemical abundances, not all of the plasma components may be relevant. For example, in studies of the composition of the ejecta of the progenitor star, it is vital to assure that only those components that were part of the progenitor star are considered. Tsamis et al. (2011), Tsamis & Walsh (2011) and Mesa-Delgado et al. (2012) provide

an enlightening study, though for a different context (a proplyd in Orion).

In planetary nebulae, there are multiple ways of incorporating external material whose origin is not the progenitor star. A simple example is the sweeping up of interstellar material during the evolution of the nebular shell (e.g., Villaver et al. 2002). Although this mechanism could be relevant for relatively evolved objects when the shell is optically-thin and the analysis includes swept up interstellar material, it cannot explain the kinematics we find for the C II, N II, O II, and Ne II lines in NGC 7009. The dust discs found around the central stars of some planetary nebulae could be a more relevant example of external material (Su et al. 2007; Chu et al. 2011; Bilíková et al. 2012), which Henney & Stasińska (2010) find may be responsible for the chemical abundances in the surrounding nebulae under some circumstances. In this scenario, the kinematics of the ORLs need not coincide with those expected from ionization equilibrium, as the sublimating material will be at least partially decoupled from the nebular shell, and so could be compatible with our observations in NGC 7009. In both cases, the external material is relevant to determine the composition of the nebular plasma, but not that of the matter ejected by the progenitor star.

The foregoing has far-reaching consequences concerning nebular abundances throughout the universe. However, NGC 7009 belongs to a minority group of planetary nebulae with large ADFs (approximately 20% of the total; Liu 2010) that generally have densities and sizes implying that they are not very young (Robertson-Tessi & Garnett 2005). The frequency of planetary nebulae with dust discs is similar (17%; Bilíková et al. 2012), though based upon a small sample. On the other hand, most planetary nebulae and almost all H II regions have ADFs of about a factor of 2 (García-Rojas & Esteban 2007; Liu 2010) and it is unclear whether the ADF phenomenon in these objects has the same origin as in the planetary nebulae with large ADFs (García-Rojas & Esteban 2007). Clearly, it would be worthwhile further investigating the kinematics and spatial distributions of ORLs in objects spanning a large range in ADF and nebular excitation.

5. Conclusions

We analyze spatially- and velocity-resolved spectroscopy of NGC 7009 obtained with the UVES spectrograph at the ESO VLT (UT2) to study the kinematics of its emission lines. We construct position-velocity maps for emission lines arising from different physical mechanisms and for the physical conditions.

We are able to study the ionization structure for oxygen in exquisite detail: O^{3+} via O III $\lambda 3707$, the transition zone to O^{2+} via O III $\lambda 3444$ (Bowen fluorescence) and O III $\lambda\lambda 3757, 5592$ (charge transfer), the O^{2+} zone via [O III] $\lambda\lambda 4363, 4959$ (collisional excitation) and O II $\lambda\lambda 4639, 4649$ (recombination), the O^+ zone via [O II] $\lambda\lambda 3726, 3729$, and the outermost H transition zone via [O I] $\lambda 6300$. The *only* anomaly is that the kinematics of the collisionally-excited [O III] $\lambda\lambda 4363, 4959$ lines does not coincide with that of the O II $\lambda\lambda 4639, 4649$ recombination lines. The kinematics favor at least two emission components for the O II $\lambda\lambda 4639, 4649$ recombination lines. The plasma from which a large fraction of the O II emission arises clearly does not originate within the volume expected from the viewpoint of ionization equilibrium as traced by the [O III] emission (§§3.1 and 4.2, Fig. 11). Instead, it arises from a zone interior to it. There is also a widely-distributed plasma component, co-spatial with the collisional [O III] emission, that also gives rise to O II $\lambda\lambda 4639, 4649$ recombination emission.

The C II, N II, and Ne II recombination lines appear to follow the distribution of the O II lines. (Their PV diagrams are usually of lower signal-to-noise.) So, in NGC 7009, a large fraction of the C II, N II, O II, and Ne II recombination emission appears to arise internal to the zone expected to contain the doubly-ionized parent ions. This result is in agreement with studies of the spatial distributions of recombination and forbidden lines (see §4.2) that typically find that the former are more centrally-concentrated.

The kinematics of the C II, N II, O II, and Ne II recombination lines in NGC 7009 clearly favor a separate plasma component emitting mostly (only?) in these lines. In NGC 7009, this plasma component would be metal-rich (as opposed to H-poor) since it is not a strong emitter in He I lines. We are unable to find unambiguous kinematic ev-

idence for the existence of metal-rich clumps (e.g., Liu et al. 2000), but cannot rule them out. Other explanations for the origin of the C II, N II, O II, and Ne II lines, such as temperature fluctuations or modifications of atomic physics are either ruled out or implausible for NGC 7009 considering the kinematics we observe.

The existence of multiple plasma components has very important consequences for the calculation and interpretation of chemical abundances. Given the kinematics we find for NGC 7009, the discrepant abundances inferred from forbidden and recombination lines pertain to different plasma components within the nebula. In NGC 7009, the “abundance discrepancy” arises because these plasma components have different chemical compositions and are probed by emission lines excited by different mechanisms. Until we understand the origin of these plasma components, the interpretation of their chemical composition will be ambiguous. There is no doubt that both components are present within the nebula in gaseous form. However, both may not be relevant for all astrophysical purposes, particularly if these purposes pertain to the composition of the ejecta of the progenitor star.

As regards the physical conditions and chemical abundances derived from collisionally-excited lines in NGC 7009, we find few problems that could prevent their use to reliably measure the chemical composition of the plasma component from which they arise. The only surprise we find is that we directly observe a recombination contribution to the [N II] $\lambda 5755$ line that is often used as a temperature indicator in ionized nebulae. Once this is accounted for, the [O III], [Ne III], and [N II] temperatures agree. The [Ar IV] and [O II] densities present a coherent picture of the structure seen in direct images. These results indicate that the atomic data for these species should be reliable. We therefore conclude that forbidden lines provide reliable chemical abundances for the plasma component from which they arise.

Finally, we recommend further study of the kinematics of recombination lines to determine whether the kinematics we find for the C II, N II, O II, and Ne II lines in NGC 7009 is a common phenomenon. Likewise, further study to determine the frequency of dust discs around the central stars of planetary nebulae would be very useful to

ascertain whether these could be an explanation for the ADF phenomenon, at least in planetary nebulae with large ADFs (Bilíková et al. 2012).

We acknowledge financial support throughout this project from CONACyT grants 43121, 49447, 82066, 106719, and 129753 and from UNAM-DGAPA grants IN105511, IN108406, IN110011, and IN116908. This research has made use of the SIMBAD database, operated at CDS, Strasbourg, France. We thank José Alberto López and the anonymous referee for helpful comments.

REFERENCES

- Aller, L. H. 1984, *Physics of Gaseous Nebulae* (Dordrecht, the Netherlands: D. Reidel Publishing Co.)
- Barker, T. 1982, *ApJ*, 253, 167
- Barker, T. 1991, *ApJ*, 371, 217
- Barlow, M. J., Hales, A. S., Storey, P. J., Liu, X.-W., Tsamis, Y. G., & Aderin, M. E. 2006, in *Planetary Nebulae in our Galaxy and Beyond*, Proceedings IAU Symp. 234 (ed. M. J. Barlow & R. H. Méndez), 367
- Bilíková, J., Chu, Y.-H., Gruendl, R. A., Su, K. Y. L., & De Marco, O. 2012, *ApJS*, 200, 3
- Bohigas, J. 2009, *Rev. Mexicana Astron. Astrofis.*, 45, 107
- Bohigas, J., López, J. A., & Aguilar, L. 1994, *A&A*, 291, 595
- Bowen, I. S. 1960, *ApJ*, 132, 1
- Chu, Y.-H., Su, K. Y. L., Bilíková, J., Gruendl, R. A., De Marco, O., Guerrero, M. A., Updike, A. C., Volk, K., & Rauch, T. 2011, *AJ*, 142, 75
- Clegg, R. E. S., Miller, S., Storey, P. J., & Kisielius, R. 1999, *A&AS*, 135, 359
- Esteban, C., Peimbert, M., García-Rojas, J., Ruiz, M. T., Peimbert, A., & Rodríguez, M. 2004, *MNRAS*, 355, 229
- Fang, X., & Liu, X.-W. 2011, *MNRAS*, 415, 181
- Fang, X., & Liu, X.-W. 2012, arXiv:1212.0005
- Ferland, G. J., Porter, R. L., van Hoof, P. A. M., Williams, R. J. R., Abel, N. P., Lykins, M. L., Shaw, G., Henney, W. J., & Stancil, P. C. 2013, *Rev. Mexicana Astron. Astrofis.*, 49, 137
- Fillipenko, A. 1982, *PASP*, 94, 715
- García-Rojas, J., & Esteban, C. 2007, *ApJ*, 670, 457
- Garnett, D. R., & Dinerstein, H. L. 2001a, *ApJ*, 558, 145
- Gonçalves, D. R., Corradi, R. L. M., Mampaso, A., & Perinotto, M. 2003, *ApJ*, 597, 975
- Grandi, S. A. 1976, *ApJ*, 206, 658
- Henney, W. J., & Stasińska, G. 2010, *ApJ*, 711, 881
- Kaufman, V., & Sugar, J. 1986, *J. Phys. Chem. Ref. Data* 15, 321
- Liu, X.-W. 2006, in *Planetary Nebulae in our Galaxy and Beyond*, Proceedings IAU Symp. 234 (ed. M. J. Barlow & R. H. Méndez), 219
- Liu, X.-W. 2010, in *New Vision 400: Engaging Big Questions in Astronomy and Cosmology Four Hundred Years after the Invention of the Telescope*, eds. D. G. York, O. Gingerich, S.-N. Zhang, and C. L. Harper, Jr; also arXiv:1001.3715v2
- Liu, X.-W., Barlow, M. J., Zhang, Y., Bastin, R. J., & Storey, P. J. 2006, *MNRAS*, 368, 1959
- Liu, X.-W., & Danziger, I. J. 1993, *MNRAS*, 261, 465
- Liu, X.-W., Luo, S. G., Barlow, M. J., Danziger, I. J., & Storey, P. J. 2001, *MNRAS*, 327, 141
- Liu, X.-W., Storey, P. J., Barlow, M. J., & Clegg, R. E. S. 1995, *MNRAS*, 272, 369
- Liu, X.-W., Storey, P. J., Barlow, M. J., Danziger, I. J., Cohen, M., & Bryce, M. 2000, *MNRAS*, 312, 585
- Liu, Y., Liu, X.-W., Luo, S.-G., & Barlow, M. J. 2004, *MNRAS*, 353, 1231

- Luo, S. G., & Liu, X.-W. 2003 in IAU Symp. 209, Planetary Nebulae: Their Evolution and Role in the Universe, eds. S. Kwok, M. A. Dopita, & R. Sutherland (Astronomical Society of the Pacific: San Francisco), 393
- Luo, S. G., Liu, X.-W., & Barlow, M. J. 2001, MNRAS, 326, 1049
- McLaughlin, B. M., & Bell, K. L. 1993, ApJ, 408, 753
- Mesa-Delgado, A., Esteban, C., García-Rojas, J. 2008, ApJ, 675, 389
- Mesa-Delgado, A., Esteban, C., García-Rojas, J., Luridiana, V., Bautista, M., Rodríguez, M., López-Martín, L., Peimbert, M. 2009b, MNRAS, 395, 855
- Mesa-Delgado, A., López-Martín, L., Esteban, C., García-Rojas, J., & Luridiana, V. 2009a, MNRAS, 394, 693
- Mesa-Delgado, A., Núñez-Díaz, M., Esteban, C., García-Rojas, J., Flores-Fajardo, N., López-Martín, L., Tsamis, Y. G., & Henney, W. J. 2012, MNRAS, 426, 614
- Mesa-Delgado, A., Núñez-Díaz, M., Esteban, C., López-Martín, L., & García-Rojas, J. 2011, MNRAS, 417, 420
- Nicholls, D. C., Dopita, M. A., & Sutherland, R. S. 2012, ApJ, in press; also arXiv:1204.3880
- Nussbaumer, H., & Rusca, C. 1979, A&A, 72, 129
- Nussbaumer, H., & Storey, P. J. 1981, A&A, 99, 177
- Nussbaumer, H., & Storey, P. J. 1984, A&AS, 56, 293
- Osterbrock, D. E. 1989, Astrophysics of Gaseous Nebulae and Active Galactic Nuclei (Mill Valley, USA: University Science Books)
- Otsuka, M., Hyung, S., Lee, S.-J., Izumiura, H., & Tajitsu, A. 2009, ApJ, 705, 509
- Otsuka, M., Tajitsu, A., Hyung, S., & Izumiura, H. 2010, ApJ, 723, 658
- Peimbert, M. 1967, ApJ, 150, 825
- Peimbert, M., & Peimbert, A. 2006, in Planetary Nebulae in our Galaxy and Beyond, Proceedings IAU Symp. 234 (ed. M. J. Barlow & R. H. Méndez), 227
- Perinotto, M., Schönberner, D., Steffen, M., & Calonaci, C. 2004, A&A, 414, 993
- Phillips, J. P., Cuesta, L. C., & Ramos-Larios, G. 2010, MNRAS, 409, 881
- Pradhan, A. K., Nahar, S. N., Eissner, W. B., & Montenegro, M. 2011, BAAS, 43, 440
- Ralchenko, Yu., Kramida, A., Reader, J. and NIST ASD Team (2011). NIST Atomic Spectra Database (version 4.1), [Online]. Available: <http://physics.nist.gov/asd>, National Institute of Standards and Technology, Gaithersburg, MD
- Rauch, T. 2003, A&A, 403, 709
- Robertson-Tessi, M., & Garnett, D. R. 2005, ApJS, 157, 371
- Rodríguez, M., & García-Rojas, J. 2010, ApJ, 708, 1551
- Rubin, R. H., Bhatt, N. J., Dufour, R. J., Buckalew, B. A., Barlow, M. J., Liu, X.-W., Storey, P. J., Balick, B., Ferland, G. J., Harrington, J. P., & Martin, P. G. 2002, MNRAS, 334, 777
- Sabbadin, F., Turatto, M., Cappellaro, E., Benetti, S., & Ragazzoni, R. 2004, A&A, 416, 955
- Sharpee, B., Baldwin, J., & William, R. 2004, ApJ, 615, 323
- Steffen, W., Espíndola, M., Martínez, S., & Koning, N. 2009, Rev. Mexicana Astron. Astrofis., 45, 143
- Su, K. Y. L., Chu, Y.-H., Rieke, G. H. et al. 2007, ApJ, 657, 41
- Tsamis, Y. G., Barlow, M. G., Liu, X.-W., Danziger, I. J., & Storey, P. J. 2003, MNRAS, 345, 186
- Tsamis, Y. G., & Walsh, J. R. 2011, MNRAS, 417, 2072

- Tsamis, Y. G., Walsh, J. R., Péquignot, D., Barlow, M. J., Danziger, I. J., & Liu, X.-W. 2008, MNRAS, 386, 22
- Tsamis, Y. G., Walsh, J. R., Vílchez, J. M., & Péquignot, D. 2011, MNRAS, 412, 1367
- Villaver, E., Manchado, A., & García-Segura, G. 2002, ApJ, 581, 1204
- Wesson, R., Liu, X.-W., & Barlow, M. G. 2005, MNRAS, 362, 424
- Wiese, W. L., Fuhr, J. R., & Deters, T. M. 1996, J. Phys. Chem. Ref. Data, Monograph 7
- Wilson, O. C. 1950, ApJ, 111, 279
- Wyse, A. B. 1942, ApJ, 95, 356
- Zeippen, C. J., Butler, K., & Le Bourlot, J. 1987, A&A, 188, 251

TABLE 1
ADOPTED LINE WAVELENGTHS

Line	Wavelength (Å)	Splitting (km/s)
optical recombination lines		
H β	4861.320	39.2
H α	6562.791	39.4
He I λ 4922	4921.931	40.1
He II λ 4686	4685.748	33.1
C II λ 4267	4267.261	35.4
C II λ 6578	6578.05	36.0
N II λ 5680	5679.56	35.1
O II λ 4639	4638.856	36.6
O II λ 4649	4649.135	35.5
Ne II λ 3335	3334.837	35.1
Ne II λ 3694	3694.215	38.0
N III λ 4379	4379.11	34.1
O III λ 3707	3707.24	34.0
collisionally-excited lines		
[N II] λ 5755	5754.57	37.8
[N II] λ 5755 recomb.	5754.57	36.0
[N II] λ 6583	6583.39	41.5
[O I] λ 6300	6300.32	
[O II] λ 3726	3726.05	40.4
[O II] λ 3729	3728.80	41.7
[O III] λ 4363	4363.21	37.1
[O III] λ 4959	4958.92	39.2
[Ne III] λ 3869	3868.76	38.2
[Ar IV] λ 4711	4711.34	36.0
[Ar IV] λ 4740	4740.20	35.7
Bowen fluorescence lines		
N III λ 4641	4640.64	36.2
O III λ 3444	3444.10	34.8
charge transfer lines		
O III λ 5592	5592.37	35.2
O III λ 3757	3757.21	34.9

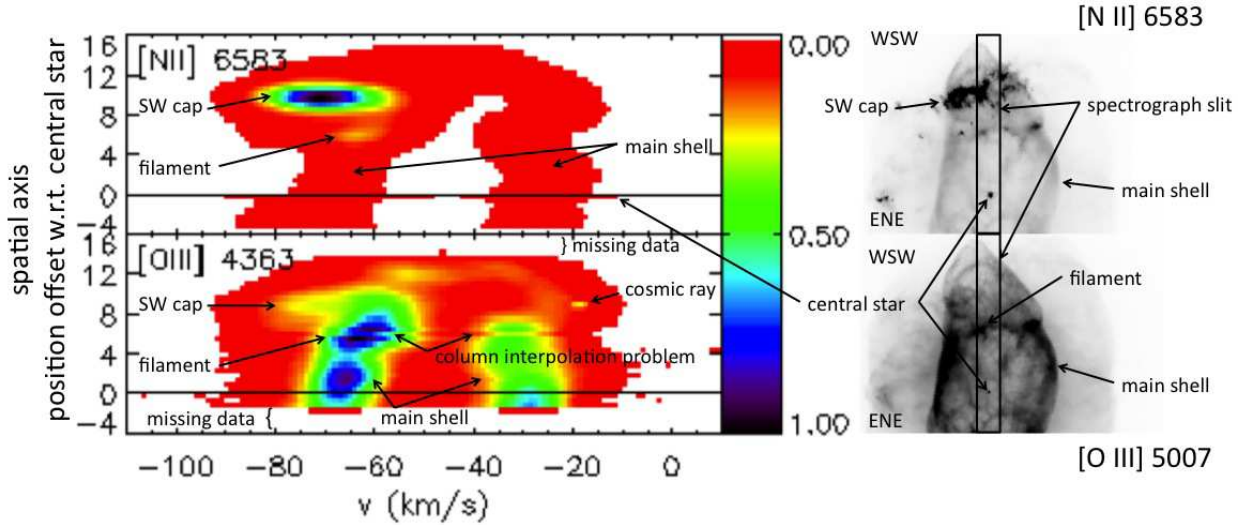


Fig. 2.— We present PV diagrams and images for NGC 7009 with the same spatial scale to illustrate their correspondence. The HST WFPC2 images in [N II] $\lambda 6583$ (top) and [O III] $\lambda 5007$ (bottom) indicate the combined position of the UVES slits (spatial directions indicated). For the PV diagrams, the spatial axis is the vertical direction and the velocity axis has the most negative velocities (blue-shifted) on the left. The color scale spans the range of 0%-100% of the maximum intensity in both PV diagrams. The white level extends to 1% of the maximum intensity. The horizontal black line in the PV diagrams indicates the position of the central star. Morphological structures from Sabbadin et al. (2004) are indicated. In the [N II] $\lambda 6583$ PV diagram (left), the brightest feature is the SW cap, the filament is considerably fainter, and the main shell is very faint. There is faint remnant emission from the central star. Except for the central star, the same emission components are visible in the [O III] $\lambda 4363$ PV diagram (right), but the relative intensities differ, in agreement with their intensities in the direct images, e.g., the filament is now brightest. We choose this PV map rather than [O III] $\lambda\lambda 4959, 5007$ to show the smaller spatial coverage of the UVES blue arm as well as the interpolation problem between the two slit positions that affects all of the blue spectra (and apparently splits the filament). From the PV diagrams, we infer that the SW cap and filament are on the side of the nebula closest to Earth (blue-shifted).

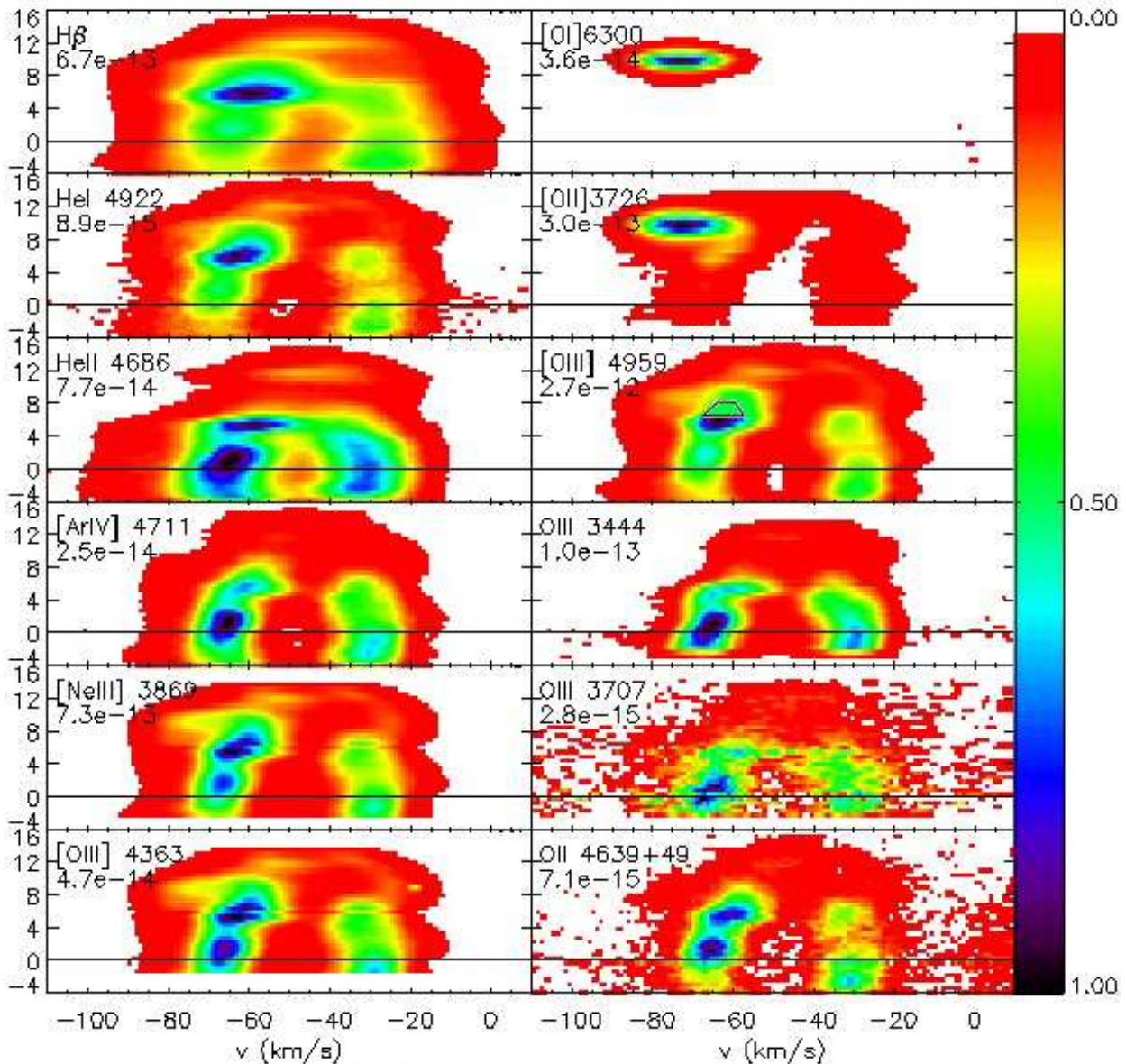


Fig. 3.— We present PV diagrams for NGC 7009 in the light of different emission lines. In each panel, the emission line and maximum intensity are identified in the upper left. The color scale spans the range of 0%-100% of the maximum intensity. The white level extends to 2% of the maximum intensity. The spatial scale is indicated on the left, measured in seconds of arc from the position of the central star (indicated by the horizontal line). The radial velocity scale spans from -110 to +10 km s^{-1} (no heliocentric correction). The spatial region used to measure the velocity splitting in Table 1 spans the spatial range from +0''5 to +2''5, immediately above/SW of the central star. The emission at positive velocities in the O II $\lambda\lambda 4639, 4649$ PV diagram is due to the nearby C III $\lambda 4650$ line (see Fig. 4). The trapezoid in the [O III] $\lambda 4959$ PV diagram indicates the region (part of the filament; Fig. 2) where the flux in this line is saturated.

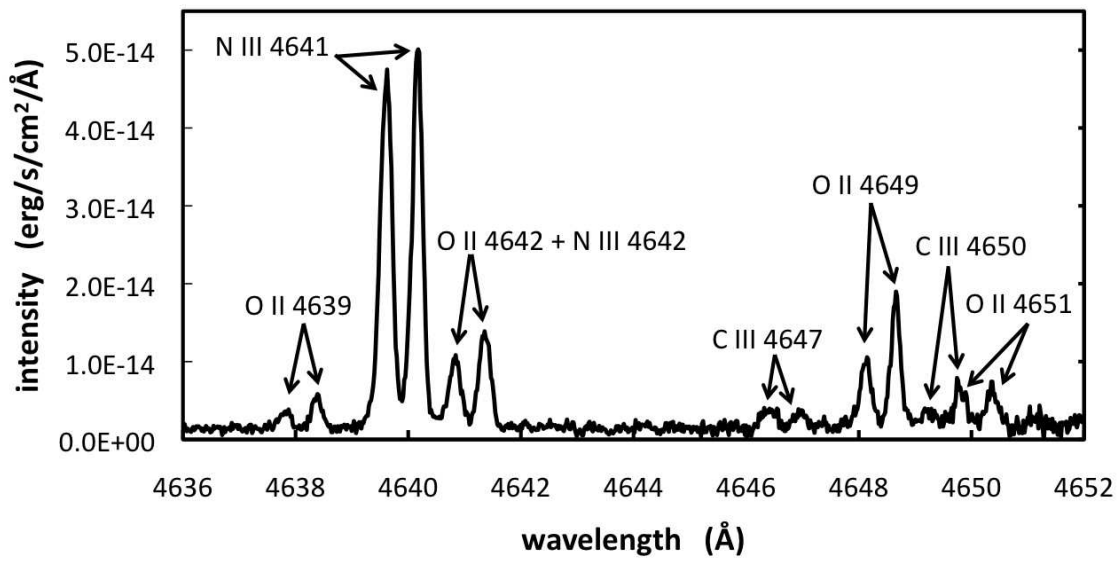


Fig. 4.— We present the spectrum around the O II $\lambda\lambda$ 4639,4642,4649,4651 lines. The O II $\lambda\lambda$ 4639,4649 lines are not blended with N III or C III lines though the O II $\lambda\lambda$ 4642,4651 lines are affected.

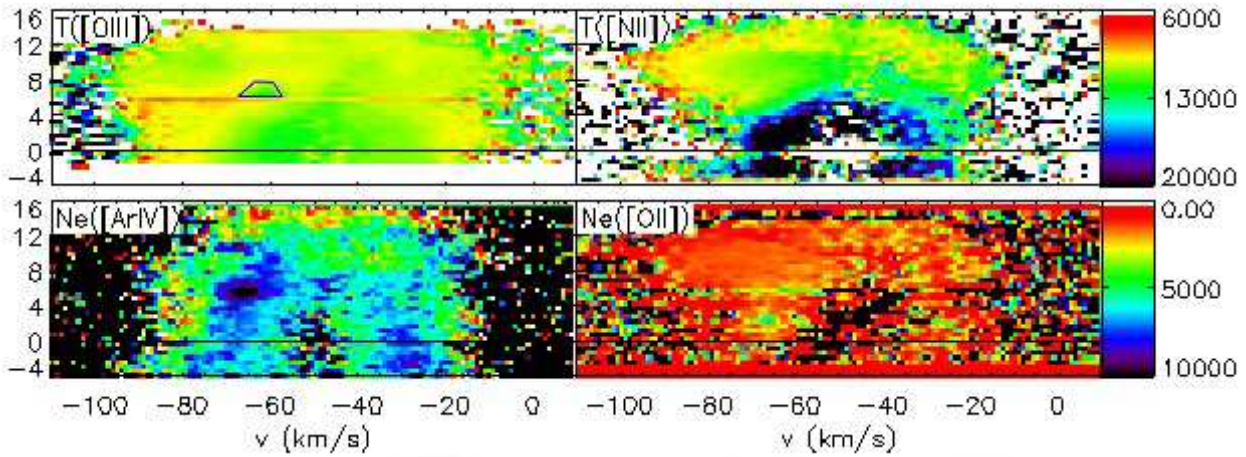


Fig. 5.— We present PV diagrams for the [O III] and [N II] temperatures (top: left and right, respectively) and the [Ar IV] and [O II] densities (bottom: left and right, respectively). The [O III] and [N II] temperatures agree in the top part of the PV diagram, with temperatures varying by about 600 K about a value of 10,000 K, but differ by about a factor of two in the bottom part of the diagram. The [Ar IV] density map is quite uniform throughout the main shell, except at the position of the filament (Fig. 2), which has a higher density. The low ionization material visible in [O II] $\lambda 3726$, including the SW cap (Fig. 2) and that interior to the Ar^{3+} zone is of substantially lower density. The trapezoid (top left) indicate the saturated region in the [O III] $\lambda 4959$ PV diagram. The white level extends to 6,390 K in the top row and to 300 cm^{-3} in the bottom row. See Fig. 3 for further details.

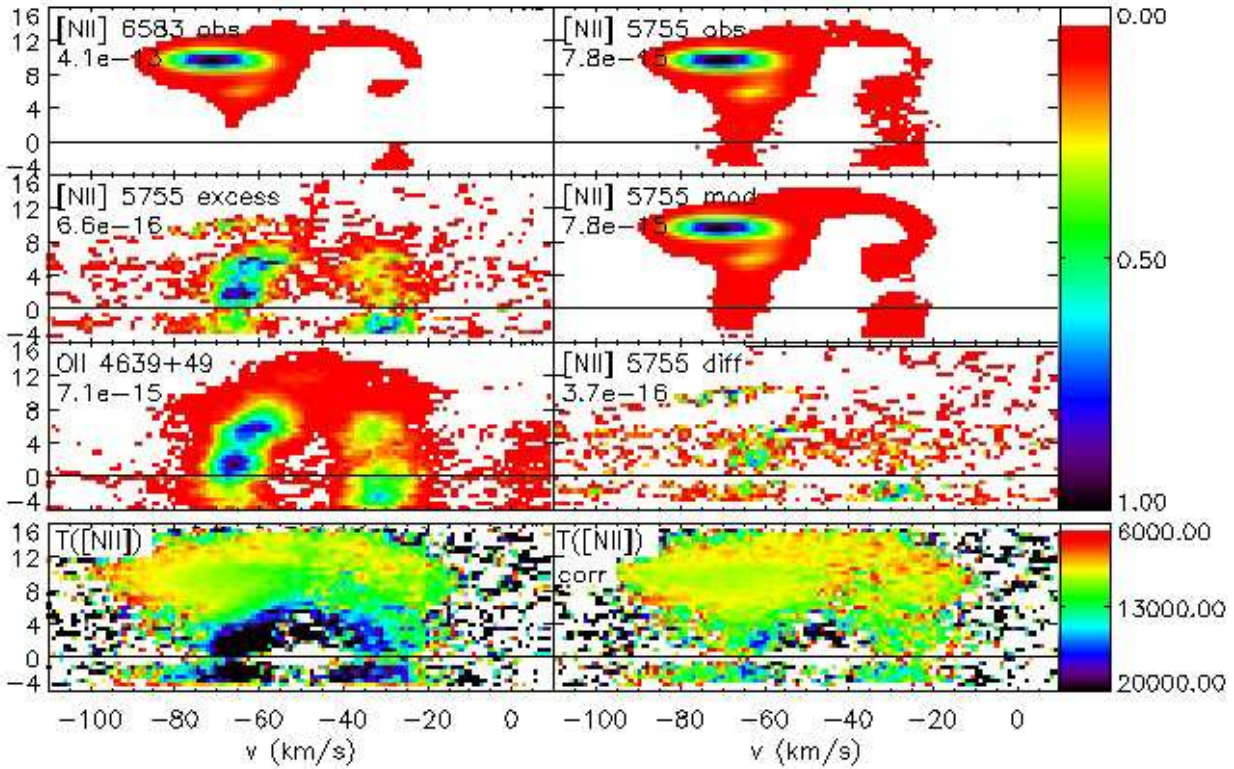


Fig. 6.— We present observed and modeled PV diagrams for the [N II] $\lambda\lambda 5755, 6583$ and O II $\lambda\lambda 4639, 4649$ lines. The modeled [N II] $\lambda 5755$ map is constructed by adding a scaled O II $\lambda\lambda 4639, 4649$ map to the scaled [N II] $\lambda 6583$ map (see text). The map of the [N II] $\lambda 5755$ excess is obtained by subtracting a scaled [N II] $\lambda 6583$ map from the observed [N II] $\lambda 5755$ map. The PV diagram of the excess emission is very similar to the O II $\lambda\lambda 4639, 4649$ PV diagram. At right in the third row is the difference of the observed [N II] $\lambda 5755$ map and the modeled map. The residuals are less than 10% of the maximum intensity of the [N II] $\lambda 5755$ map, which confirms that the excess [N II] $\lambda 5755$ emission coincides closely with that of O II $\lambda\lambda 4639, 4649$. In the bottom row are maps of the [N II] temperature using the [N II] $\lambda 5755$ PV diagram as observed (left) and after subtracting the scaled O II $\lambda\lambda 4639, 4649$ PV diagram (right). The white level extends to 3% of the maximum intensity in top three rows and to 6,390 K in the bottom row. See Fig. 3 for further details.

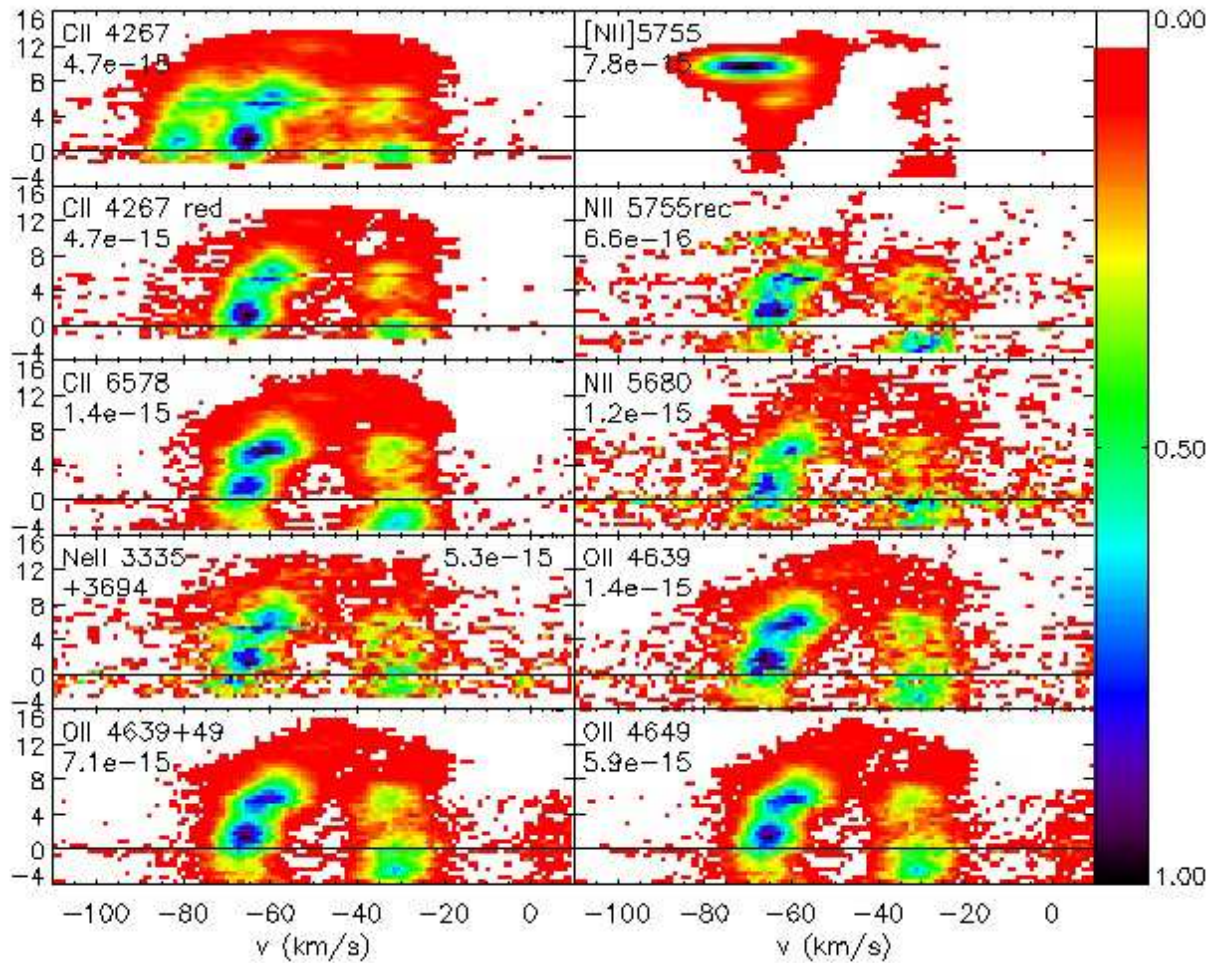


Fig. 7.— The PV diagrams in C II, N II, O II, and Ne II recombination lines are strikingly similar. Excepting C II 6578, even the relative intensities of the different components are the same: the blue-shifted emission is always brighter than the red-shifted emission and the components closest to the central star are brighter than the more distant components. The PV diagrams in the second row are derived from those in the first row (see text). C II 6578 and N II 5680 can be excited via recombination or by indirect continuum fluorescence. The white level extends to 4% of the maximum intensity. See Fig. 3 for further details. In the panel for Ne II 3335 + 3694, the maximum intensity is shown at upper right for clarity.

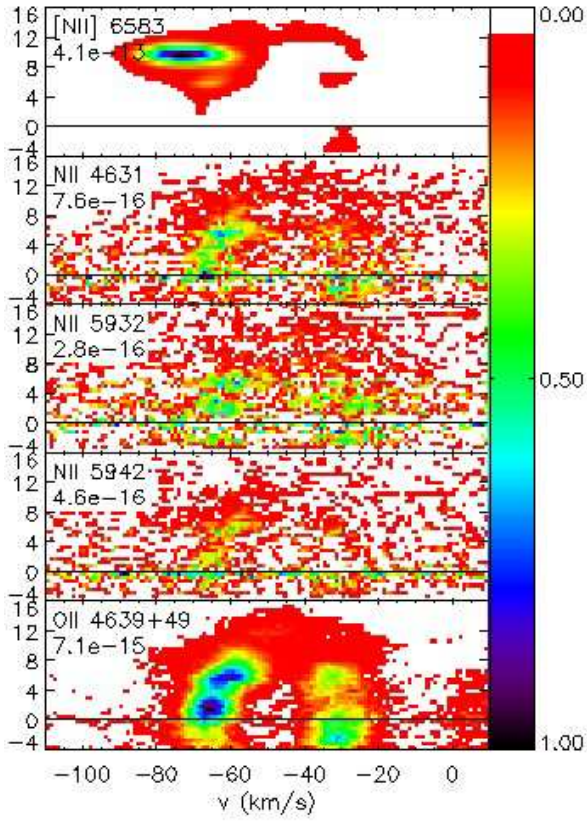


Fig. 8.— We compare the collisionally-excited [N II] $\lambda 6583$ line with the N II $\lambda\lambda 4631, 5932, 5942$ lines that can be excited via fluorescence and the O II $\lambda\lambda 4639, 4649$ recombination lines. In spite of the low signal-to-noise, the N II $\lambda\lambda 4631, 5932, 5942$ PV diagrams are more similar to that of O II $\lambda\lambda 4639, 4649$, indicating that this process likely dominates their production in NGC 7009. The white level extends to 3% of the maximum intensity. See Fig. 3 for further details.

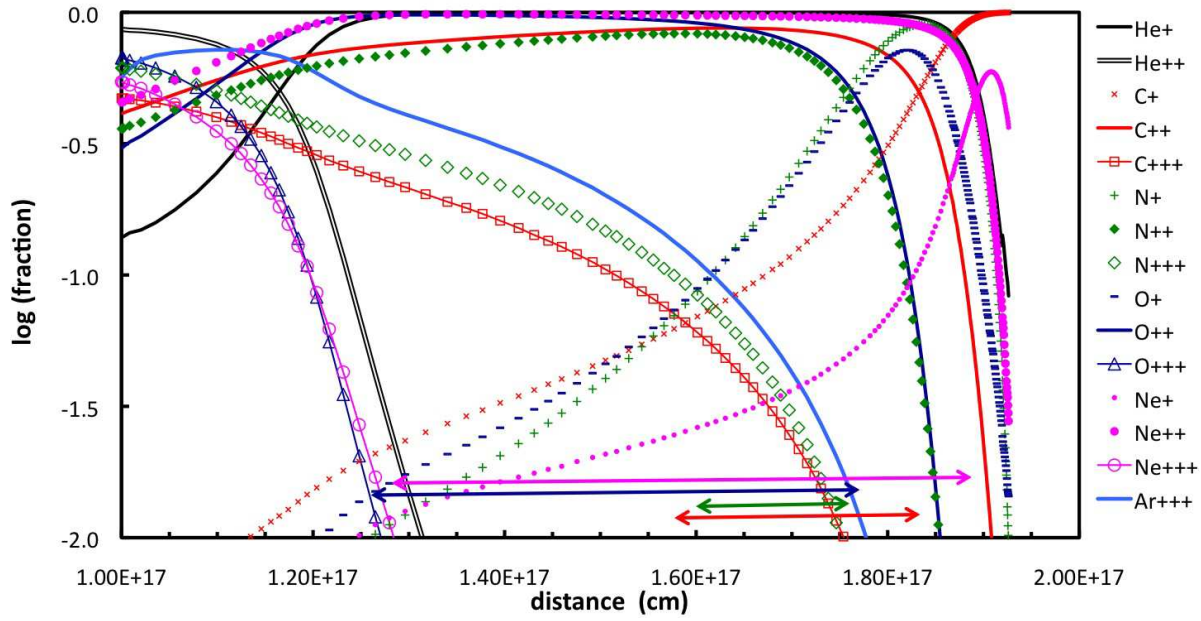


Fig. 9.— We plot the fractional ionization in a model nebula as a function of distance from the ionizing source. This optically-thick model was computed using v08.00 of CLOUDY, last described by Ferland et al. (2013), assuming an inner radius of 10^{17} cm (Sabbadin et al. 2004, their Fig. 9, top panel), a constant density of 4000 cm^{-3} , a filling factor of unity, a homogeneous chemical composition (CLOUDY’s default abundance set for planetary nebulae), and a stellar atmosphere model from Rauch (2003, 100,000 K, $\log g = 5$, $\log L_{bol} = 38.6$). The red, green, blue, and magenta arrows at bottom indicate the zones from which emission should arise from C II, N II, O II, and Ne II, respectively.

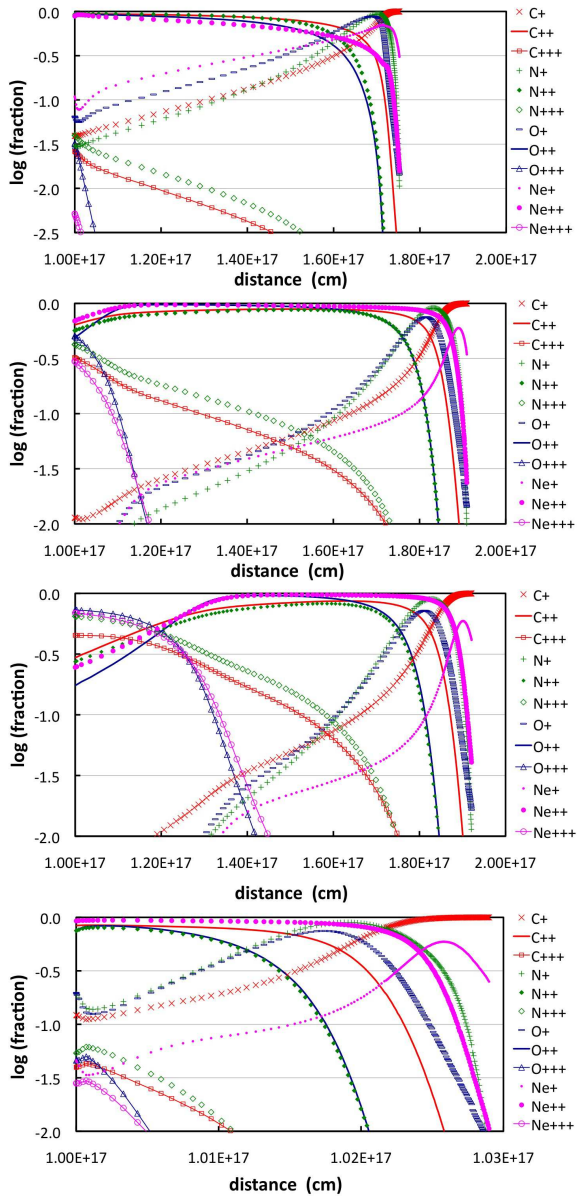


Fig. 10.— We present additional models whose parameters are varied from those in Fig. 9. In the top three panels, the central stars are modeled as black bodies with temperatures of 60,000 K (top), 80,000 K (second), and 120,000 K (third). In the bottom panel, the density is increased by a factor of 10 (note the change in horizontal scale). Otherwise, the parameters are as in Fig. 9. For clarity, we omit the He^{2+} , He^+ , and Ar^{3+} ionization fractions.

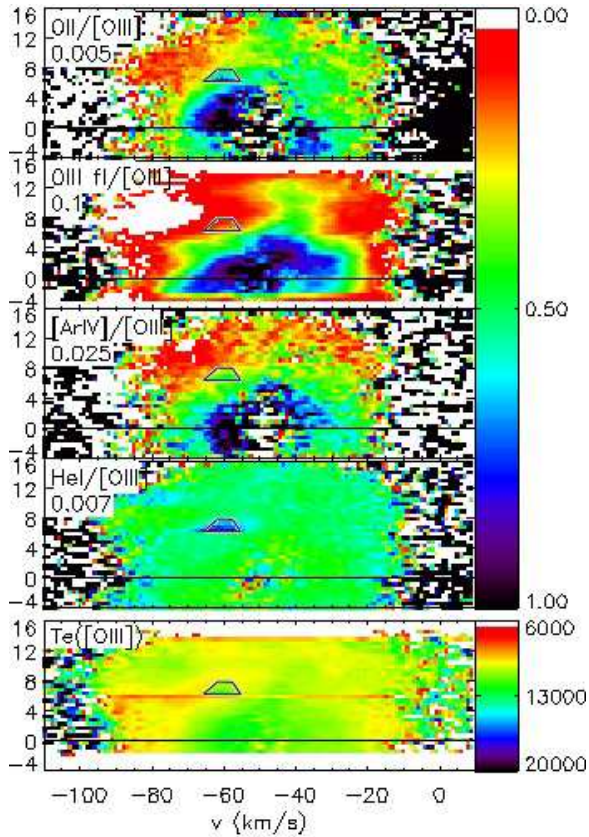


Fig. 11.— These PV diagrams present ratios of O II $\lambda\lambda 4639,4649$ to [O III] $\lambda 4959$ (top), O III $\lambda 3444$ to [O III] $\lambda 4959$ (second), [Ar IV] $\lambda 4740$ to [O III] $\lambda 4959$ (third), He I $\lambda 4922$ to [O III] $\lambda 4959$ (fourth), and the [O III] temperature (bottom). The scale factor by which each ratio was normalized is given in the top four panels. Metal-rich clumps should appear as spatially-confined enhancements in the top panel. Comparing the top two panels, the O II $\lambda\lambda 4639,4649$ emission arises from a much greater part of the O²⁺ zone than does that from O III $\lambda 3444$. The first and fourth panels are very different, so the component emitting in O II $\lambda\lambda 4639,4649$ is not a strong emitter in He I $\lambda 4922$. The trapezoids indicate the saturated region in the [O III] $\lambda 4959$ PV diagram. The white level extends to 3% of the scale factor (top four panels) and to 6,390 K (bottom panel). See Fig. 3 for further details.

This figure "fig1a.png" is available in "png" format from:

<http://arxiv.org/ps/1306.6110v1>

This figure "fig1b.png" is available in "png" format from:

<http://arxiv.org/ps/1306.6110v1>

This figure "fig1c.png" is available in "png" format from:

<http://arxiv.org/ps/1306.6110v1>

This figure "fig1d.png" is available in "png" format from:

<http://arxiv.org/ps/1306.6110v1>

This figure "fig2.png" is available in "png" format from:

<http://arxiv.org/ps/1306.6110v1>

This figure "fig3.png" is available in "png" format from:

<http://arxiv.org/ps/1306.6110v1>

This figure "fig4.png" is available in "png" format from:

<http://arxiv.org/ps/1306.6110v1>

This figure "fig5.png" is available in "png" format from:

<http://arxiv.org/ps/1306.6110v1>

This figure "fig6.png" is available in "png" format from:

<http://arxiv.org/ps/1306.6110v1>

This figure "fig7.png" is available in "png" format from:

<http://arxiv.org/ps/1306.6110v1>

This figure "fig8.png" is available in "png" format from:

<http://arxiv.org/ps/1306.6110v1>

This figure "fig9.png" is available in "png" format from:

<http://arxiv.org/ps/1306.6110v1>

This figure "fig10a.png" is available in "png" format from:

<http://arxiv.org/ps/1306.6110v1>

This figure "fig10b.png" is available in "png" format from:

<http://arxiv.org/ps/1306.6110v1>

This figure "fig10c.png" is available in "png" format from:

<http://arxiv.org/ps/1306.6110v1>

This figure "fig10d.png" is available in "png" format from:

<http://arxiv.org/ps/1306.6110v1>

This figure "fig11.png" is available in "png" format from:

<http://arxiv.org/ps/1306.6110v1>